LAWRENCE
LIVERMORE
NATIONAL
LABORATORY

LLNL-JRNL-676844

Measurement and modelling of reactive transport in geological barriers for nuclear waste containment

Q. Xiong, C. Joseph, K. Schmeide, A. P. Jivkov

September 3, 2015

Physical Chemistry Chemical Physics

Disclaimer

LLNL-JRNL-676844

Measurement and modelling of reactive transport in geological barriers for nuclear waste containment

Qingrong Xiong[1], Claudia Joseph[2], Katja Schmeide[3], Andrey P Jivkov[1]

[1] Research Centre for Radwaste & Decommissioning and Modelling & Simulation Centre, Dalton Nuclear Institute, The University of Manchester, UK

[2] Glenn T. Seaborg Institute, Physical & Life Sciences Directorate, Lawrence Livermore National Laboratory, L-231, P.O. Box 808, Livermore, CA 94550, USA

[3] Helmholtz-Zentrum Dresden-Rossendorf, Institute of Resource Ecology, Bautzner Landstr. 400, 01328 Dresden, Germany

Abstract

Compacted clays are considered as excellent candidates for barriers to radionuclide transport in future repositories for nuclear waste due to their very low hydraulic permeability. Diffusion is the dominant transport mechanism, controlled by a nano-scale pore system. Assessment of the clays' long-term containment function requires adequate modelling of such pore systems and their evolution. Existing characterisation techniques do not provide complete pore space information for effective modelling, such as pore and throat size distributions and connectivity. Special network models for reactive transport are proposed here using the complimentary character of the pore space and the solid phase. This balances the insufficient characterisation information and provides the means for future mechanical-physical-chemical coupling. The anisotropy and heterogeneity of clays is represented using different length parameters and percentage of pores in different directions. Resulting networks are described as mathematical graphs with efficient discrete calculus formulation of transport. Opalinus Clay (OPA) is chosen as an example. Experimental data for the tritiated water (HTO) and U(VI) diffusion through OPA are presented. Calculated diffusion coefficients of HTO and uranium species are within the ranges of the experimentally determined data in different clay directions. This verifies the proposed pore network model and validates that uranium complexes are diffusing as neutral species in OPA. In the case of U(VI) diffusion the method is extended to account for sorption and convection. Rather than changing pore radii by coarse grained mathematical formula, physical sorption is simulated in each pore, which is more accurate and realistic.

Keywords: Reactive transport, pore network model, Opalinus Clay, pore shapes

1 Introduction

Simulation of reactive transport in both natural (soils, rocks, etc.) and industrial (concrete, bioengineered tissues, etc.) porous media is highly important to a variety of scientific and engineering applications [1-4]. These include environmental contaminant transport [1], carbon dioxide (CO_2) storage [2], bioremediation [4], and stimulation of petroleum reservoirs [5]. Most applications require further understanding of multiple processes (diffusion, convection, and reaction) and scales (microscopic and macroscopic). Because continuum reactive transport models involve averaging over length scales much larger than typical grain sizes, they are unable to resolve heterogeneity at smaller scales. This heterogeneity has been found important for reactive transport modelling at larger scales [6]. Progress can be achieved by developing physically based and microstructure-informed models suitable for such analyses. Key initial requirement is that such models are able to predict measurable transport properties at a macro-scale (engineering, geological) from measurable pore space characteristics describing structures at a meso-scale (tens of inter-pore distances).

Pore network models (PNM) are amongst the appealing approaches that provide a suitable description of mutable pore space structures. Such models have been used to describe conservative as well as reactive transport in saturated [7] or multiphase and unsaturated porous media [8, 9]. Moreover, their use has been expanded to complement the application of percolation theory to porous media [10] and to simulate the effect of microbial growth on substrate transport and system permeability [4]. The pore space is approximated by a set of sites and a set of bonds connecting some of the sites. The sites positions may form a regular lattice (regular PNM) or reflect known length variations (irregular PNM). Mass transport is allowed through the system of bonds.

Conceptually, PNM are scale indifferent, i.e. they can be applied to any length-scale interval where the structure of the pore space has been experimentally characterised. For example, if a particular experimental technique allows for characterising pore features of sizes between 0.1 μm and 10 μm, then the corresponding PNM will take these into account. The elements of PNM, sites and bonds, are abstract and can be related to the measurable features in different ways depending on the available information.

Historically, pores were related to the sites and pore throats were related to the bonds of regular PNM [11-13]. If such correspondence is to be statistically representative of the material modelled, then sufficiently rich experimental information is required: shape and size distribution of pores and throats, as well as the pore coordination spectrum, i.e. percentages of pores coordinated by different numbers of throats [13, 14]. These can be obtained from structures with distinguishable pores and pore throats. One established way is analysing 3D images from synchrotron X-ray tomography [15, 16].

It is worth mentioning, that 3D images can be used directly to construct irregular PNM [17]. These allow for validating physical assumptions for flow simulations using 4D imaging of mass transport. However, such irregular PNM are sample-specific and potentially not statistically representative. A regular PNM constructed within a larger volume allows for capturing statistics from a number of imaged samples, i.e. improved statistical correspondence, and for calculating transport at distances closer to the engineering application length scale.

X-ray computed tomography is presently limited to resolving macro-porosity (features larger than 50 nm). However, the resolution of this experimental technique is not sufficient to identify throats for systems dominated by meso-porosity (features between 5 nm and 50 nm) and micro-porosity (features smaller than 5 nm). For pore network construction, this means that pore connectivity data cannot be extracted as throats cannot be identified.

One possibility is to develop a regular PNM with pores from experimental distribution located at sites and notional throats between each pair of neighbouring pores [1] based on a topologically proper lattice proposed by Jivkov *et al.* [13]. Such a construction allows for the calculation of the lattice length scale from known porosity and pore size distribution, but the pore connectivity is constant. The diffusivity of a notional throat depends on the sizes of the connected pores, the size of the solute molecules, and the interaction of the solute with the pore walls. The approach provided insights into the effects of pore size distribution, solute size, and sorption on diffusivity [1]. It was noted, however, that the spatial randomness of pore sizes yielded variation of calculated diffusion coefficient larger than experimentally measured variability. This indicated that in the real material there was a strong connectivity effect, missed by the model due to lack of detailed information. In addition, diffusivity

114 anisotropy emerging from material texture (preferred mineral orientations) could not be
115 captured.
116
117 Another possibility is to assume variable connectivity [18]. While this was more realistic in
118 terms of pore space topology, the observable data were insufficient to establish rigorously a
119 lattice length scale. With variable length scales, improved agreement with the variability in
120 experimentally measured diffusivity was demonstrated, including diffusion anisotropy in clay.
121
122 The two approaches to tackle incomplete pore space information, namely predefined
123 connectivity for calculable length scale [1], and undetermined length scale for realistic
124 connectivity [18], suffer from the lack of an additional constraint. This cannot be found
125 within the pore space information and requires the consideration of the solid phase structure,
126 e.g., the shape and size distribution of mineral grains. A methodology for incorporating the
127 structure of the solid phase is proposed here. It improves substantially the realism of the
128 constructed PNM, both in terms of geometry and topology. The proposal has added benefit
129 that the constructed PNM can be paired directly to lattice models of the solid phase
130 developed for analysis of damage evolution via micro-cracking [19-21]. This facilitates
131 mechanistic investigations of combined mechanical-thermal-chemical-biological effects on
132 diffusivity, which will be discussed further in the paper.
133
134 Typical pore network models idealise the pore space with simple geometries, i.e. throats are
135 assumed to have square or circular cross sections. This makes it difficult to simulate
136 processes like sorption, which may change pore geometries by physical clogging. Recent
137 advances allowed to model pore geometries with irregular cross sectional shapes [8]. The
138 influence of cross sectional shapes on diffusion and sorption will be analysed in this work.
139
140 For safety assessment of repositories for high-level nuclear waste, in particular the migration
141 behaviour of radioisotopes with long half-lives (e.g., ^{238}U, $\tau_{1/2} = 4.468\times10^{9}$ a; main fraction of
142 spent nuclear fuel) is in the focus of research. Opalinus Clay (OPA) is discussed as potential
143 host rock for nuclear waste repositories, where it is considered as one of the barriers to
144 radionuclide transport, because it exhibits very low hydraulic conductivity [22]. This makes
145 molecular diffusion the main transport mechanism of radionuclides through the barrier. In the
146 present work, OPA is selected to demonstrate the development of the new pore network
147 model. The pore space information for model construction is adopted from Keller *et al.* [23,

148 24] and Nagra [22]. Validation data on macroscopic diffusivities come from [25-28].
149 Although OPA has a very low permeability, the effects of velocities on mass transport are
150 also analysed to demonstrate how the methodology will be applied to other porous media. In
151 the diffusion experiments so far the neutral $Ca_2UO_2(CO_3)_3(aq)$ complex was assumed to be
152 the main diffusing species through OPA [25], because it was spectroscopically verified to be
153 the dominant U(VI) species in the experimental source reservoir solution. The model
154 described in the present study shall clarify whether U(VI) diffuses as cationic, anionic, or
155 neutral species through OPA.
156

157 # 2 Geometric modelling and data

158

159 ## 2.1. Cellular basis for pore network construction

160

161 Statistical analysis of the neighbourhoods of arbitrary features, randomly distributed in 3D
162 space, has shown that the truncated octahedron represents the average neighbourhood [29].
163 The truncated octahedron was the unit cell of a regular space tessellation, representing the
164 neighbourhood of one type of measurable feature, a solid particle [20] or a pore [13], which
165 has been used to analyse deformation and failure of quasi-brittle media [19, 30, 31] and
166 transport in porous media [1, 18], respectively. Considering the need to couple the
167 deformation and the transport models in the future, we choose the truncated octahedron as
168 cellular basis for network construction. This has six square faces normal to three
169 perpendicular directions, say (1, 0, 0), (0, 1, 0), and (0, 0, 1), and eight hexagonal faces
170 normal to the corresponding octahedral directions, (±1, ±1, ±1).

171

172 The material is reduced to a mathematical graph by placing particles or grains at cell centres
173 (interiors). This is illustrated in Fig. 1(a) for cells with equal distances between the three pairs
174 of square faces, a setup used in the previous works. In order to represent texture anisotropy,
175 three different length parameters, S_1 [m], S_2 [m], and S_3 [m], are used to measure the
176 distances between the square faces in directions (1, 0, 0), (0, 1, 0), and (0, 0, 1), respectively.
177 All other distances are then dependent on the three length parameters, e.g., the volume of
178 each cell is $V_c = S_1 S_2 S_3 / 2$ [m^3].

179

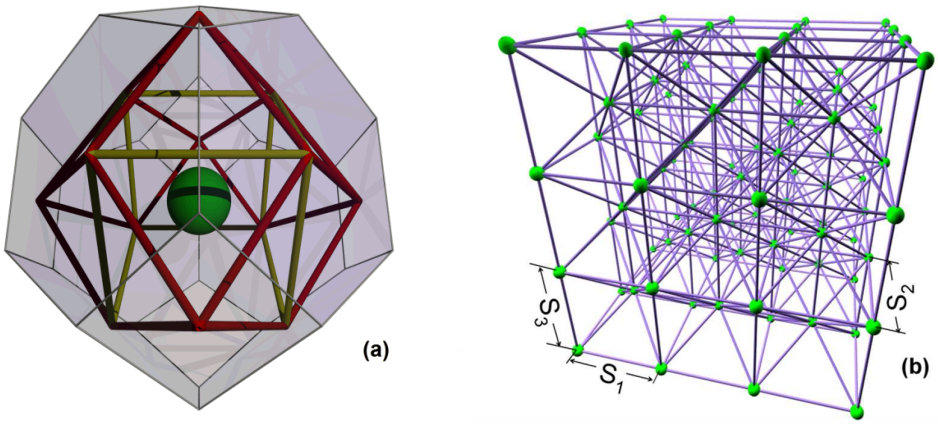

180

181 Fig. 1: Pore space representation: (a) unit cell illustrating potential diffusion paths (bonds,
182 yellow and red) in the neighbourhood of central particle (green); these join neighbouring cell

faces and show where elongated pores may be assigned to the experimental pore system information; (b) a fragment of a lattice model for deformation and failure analysis, illustrating sites on particles and bonds between neighbouring particles.

In an assembly of N_c [-] cells, each cell is assigned to a particle with different radius, r_i [m]. The assignment of particles terminates when their accumulated volume fraction equals to the experimentally measured value. From this requirement the volume of a cell assembly is calculated by:

$$V_c = \frac{1}{\phi N_c} \sum_{i=1}^{N_c} \frac{4\pi r_i^3}{3} \quad \left(= \frac{1}{2} S_1 S_2 S_3 \right) \tag{1}$$

where ϕ [-] is the measured volume percentage of particles. The calculation of the three length parameters from Eq. (1) depends on the selection of their ratios used here to represent texture. A non-textured medium has $S_1 = S_2 = S_3$.

Each particle (site, cell centre) is connected to its 14 neighbouring particles by bonds representing relative deformations between cells, illustrated in Fig. 1(b). This graph can be analysed very efficiently using discrete exterior calculus to investigate the response of the material to loading, including micro-crack generation, competition, and coalescence [32]. The presence of pores in cell neighbourhoods is reflected in pore-size-dependent reduction of bond strengths. Further, the assigned particle sizes may also contribute to spatial variation of bond properties within the model. However, for the construction of the PNM the particular particle sizes do not play a role; only the length parameter calculated by Eq. (1) is of essence.

The pore network construction is as follows. Firstly, a new skeleton is formed using sites at the centres of cell faces and bonds between neighbouring faces. This is illustrated in Fig. 1(a) on a single cell with $S_1 = S_2 = S_3$ for clarity. The bonds represent potential transport pathways, i.e. they show the positions where elongated pores are allowed to reside. Note that there are no bonds cutting through cells, hence the pore system can follow paths around particles. The elongated pores can be assigned with different cross sectional shapes, such as circular, equilateral, and square. Since pores reside on bonds, the sites at face centres represent pore junctions – volume-less containers redirecting mass transport.

Notably, this skeleton allows for pores with maximum coordination of 8 or 12 depending on whether the bond connects square to hexagonal or hexagonal to hexagonal boundary. Importantly, the length parameters of the skeleton, determining the lengths of possible pores, are now dictated by the solid phase structure.

2.2. Pore shape

A key characteristic of real porous media is the angular form of pores. It has been demonstrated that having pores with a circular cross section, and thus single-phase occupancy, causes insufficient connectivity of the wetting phase and as a result poor representation of experimental data [33]. Angular cross sections retain the wetting fluid in their corner and allow two or more fluids to flow simultaneously through the same pore. Pores which are angular in cross section are thus a more realistic model than the commonly employed cylindrical shape. The shape of an angular pore cross section is prescribed in terms of a dimensionless shape factor, G, which is defined as

$$G = \frac{A}{P^2} \tag{2}$$

where A [m^2] and P [m] are the area and the perimeter of the cross section [34], respectively. The shape factor replaces the irregular and complicated shape of a pore by an equivalent circular, triangle, or rectangle shape. The value of shape factors ranges from a minimum of zero corresponding to a slit to a maximum of 0.08 corresponding to a circular cross section. Values of shape factors for triangular cross sections vary from 0 to 0.048 (with maximum for equilateral triangle), and rectangular cross section from 0 to 0.062 (with maximum for square shape).

2.3. Assignment of porosity

Pores with the desired characteristics, e.g., porosity and pore size distribution, will be generated in a particle or grain structure that best represents the measured material's size and orientation. Usually, the pores in porous material can be divided into several groups, such as macro-pores, meso-pores, and micro-pores. For example, there exist meso-pores and micro-pores in the material. Firstly, meso-pores are assigned to available bonds of Fig. 2(a) according to the experimental data. An available bond is a bond with no previously assigned

pore. The volume of all allocated meso-pores is required to equal experimentally determined meso-pore volume, i.e. when

$$\sum_i V_i = N_c \, V_c \, \theta_{mes} \tag{3}$$

where V_i [m^3] is the pore volume, θ_{mes} [-] is the volume fraction of meso-pores. The assignment of meso-pores can be in different directions or constrained to a selected direction, to simulate the anisotropy and heterogeneity. In the selected direction, the pores are randomly assigned to bonds. All bonds in the chosen direction are available for meso-pore assignment.

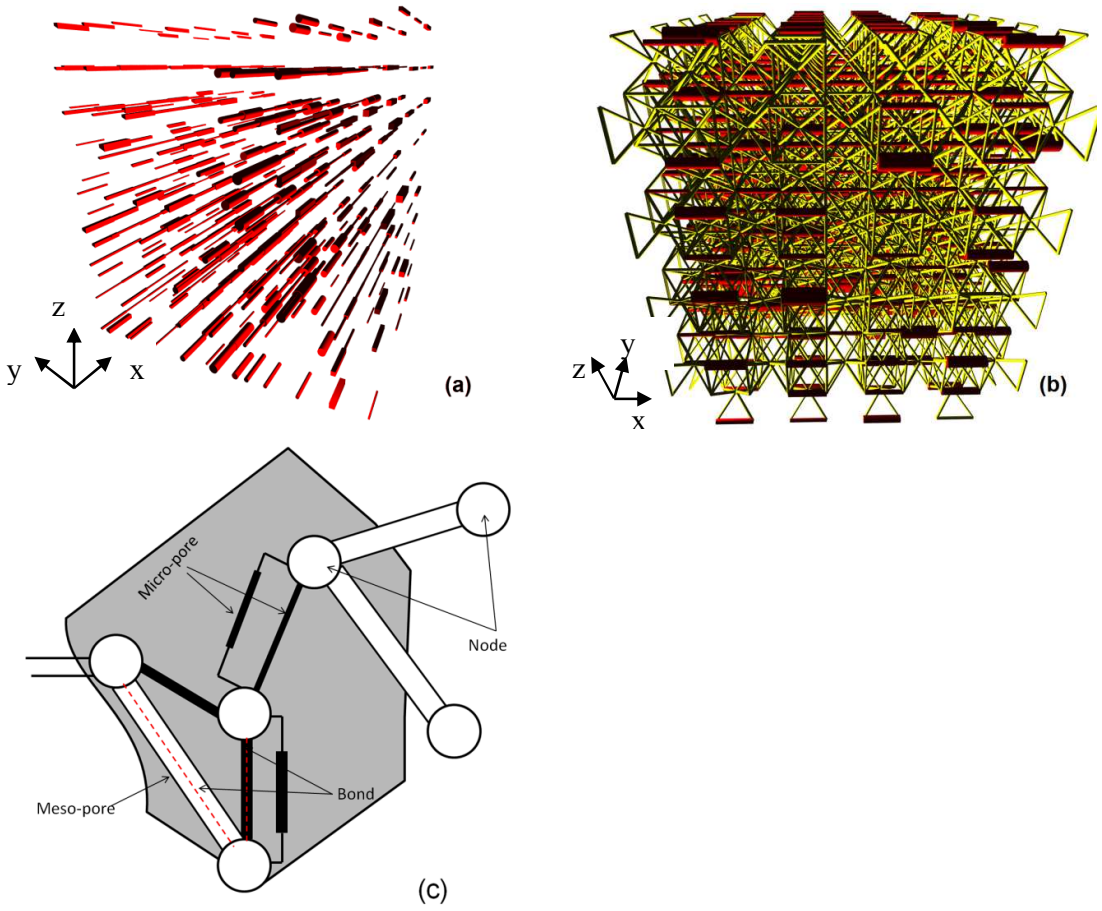

Fig. 2: Illustration of pore assignment to diffusion site-bond model: (a) exclusive assignment of meso-pores along (1, 0, 0) with different pore cross sectional shapes taken as the clay bedding direction; (b) pore network model after assignment of meso-pores (red) and micro-pores (yellow) – micro-pores allowed in all directions. Examples are given on lattice with equal length parameters for bedding and out-of-bedding directions. (c) Schematic depiction of meso-pores and micro-pores assigned to bonds.

Secondly, micro-pores are assigned to bonds not already occupied by meso-pores. The micro-pores are also assumed to be of different shape and each new pore assignment increments the pore volume according to selected cross section area and bond length. The process terminates when the total pore volume fraction, from meso- and micro-pores, attains the experimental porosity. Notably, micro-pores are allowed at bonds in all directions, including bonds in the bedding direction not occupied by meso-pores, and more than one micro-pore can be assigned to a bond if required to reach prescribed porosity, illustration in Fig. 2(c). A set of micro-pores assigned to a bond can be considered as providing an "effective" transport between two pore junctions, which is necessary to create transport paths in the otherwise non-percolating meso-pore system. Importantly, they act as sieves for transport of species with different molecular sizes.

An example of a PNM after assigning meso-pores and micro-pores with different pore shape sets is shown in Fig. 2(b). The micro-pore sets are presented as bundles with scaled-up cross-sections and the network is constructed with equal length parameters in the bedding and out-of bedding directions for improved illustration. In the simulations different length parameters in bedding and out-of bedding directions were used to represent texture.

2.4. Experimental characterisation data

OPA has anisotropic transport properties due to preferred orientation (or texture) of clay minerals attained during sedimentation and compaction [35]. Specifically, solute species diffuse slowly perpendicular and fast parallel to the bedding plane. Our goal is to construct a regular PNM, which calculates diffusion in line with macroscopic observations, and can be linked to models for deformation and failure of the solid phase, based on available structural data.

Regarding the pore space, we make use of the 3D analysis of OPA reported by Keller *et al.* [23, 24] and Nagra [22]. The pore space was divided into meso-pores and micro-pores based on the resolution of different experimental techniques in our work. The meso-pores were resolved by Focused Ion Beam nano-tomography (FIB-nt) with elongated pores in the bedding plane. These pores had approximately cylindrical shapes with diamaters > 10 nm and were largely isolated (i.e. solute species cannot percolate through the sample). The meso-pores occupied approximately 1.8 vol.% of the sample, i.e. their volume density (porosity)

296 was θ_{mes} = 0.018. The micro-pores were resolved by N_2 adsorption with pore sizes < 10 nm,
297 but were unresolved by FIB-nt. The analysis of N_2 adsorption gave a total physical porosity
298 of around 11.5 vol.%, of which 9.7 vol.% were micro-pores. The volume density of micro-
299 pores is thus θ_{mic} = 0.097 [23]. However, micro-pores narrower than 2 nm cannot be probed
300 by N_2 adsorption. For OPA from Mont Terri, most estimates of the total porosity are on the
301 order of 16 vol.% [25, 36, 37]. In this work, we assume that micro-pores smaller than 2 nm
302 occupy 4.5 vol.% and follow the same distribution as pores occupying 9.7 vol.%. These
303 measurements show that the fine-grained clay matrix contains an extensive micro-pore
304 network. The meso-pore system can be seen as part of the effective "flow relevant" porosity
305 that surrounds the clay mineral particles and is interconnected by micro-pores.
306
307 The two measurements were combined into a single "cumulative pore volume fraction – pore
308 radius" curve given in Fig. 3(a) [18, 23]. This shows that the geometrically resolved meso-
309 pores (symbols) and the adsorption-based curve coincide in their common length interval,
310 with meso-porosity θ_{mes} = 0.018 and total porosity θ = 0.16. The radii are derived with the
311 assumption of cylindrical pore shapes truthful to experimental evidence for meso-pores [23]
312 and approximate for micro-pores. For the purpose of model construction the experimental
313 distribution from Fig. 3(a) is re-evaluated as cumulative probability separately for meso- and
314 micro-pores. These are shown in Fig. 3(b) and Fig. 3(c), respectively. The use of the
315 cumulative probability is to produce sizes from the measured distribution in Fig. 3(a) using a
316 generator for uniformly distributed numbers $0 \leq p < 1$. This is illustrated by the red arrows on
317 Figs. 3(b) and 3(c); more details on statistics are given by Jivkov and Xiong [18]. For pores
318 with other shapes such as square, the radii are converted to length of side with equal pore
319 volume.
320
321 Regarding the structure of the solid phase, Keller *et al.* [24] reported 18 vol.% of non-porous
322 carbonates and 17 vol.% of non-porous quartz in the sample. The sizes of carbonates ranged
323 from 100 to 300 nm, while the size distribution of quartz was not measured. The reported
324 data of carbonate were converted to the cumulative probability of its grain sizes shown in Fig.
325 3(d) for model construction. The same cumulative probability is assumed for the non-porous
326 quartz, due to the lack of more accurate data, and used to generate particle sizes of both types
327 in a way similar to pore size generation.

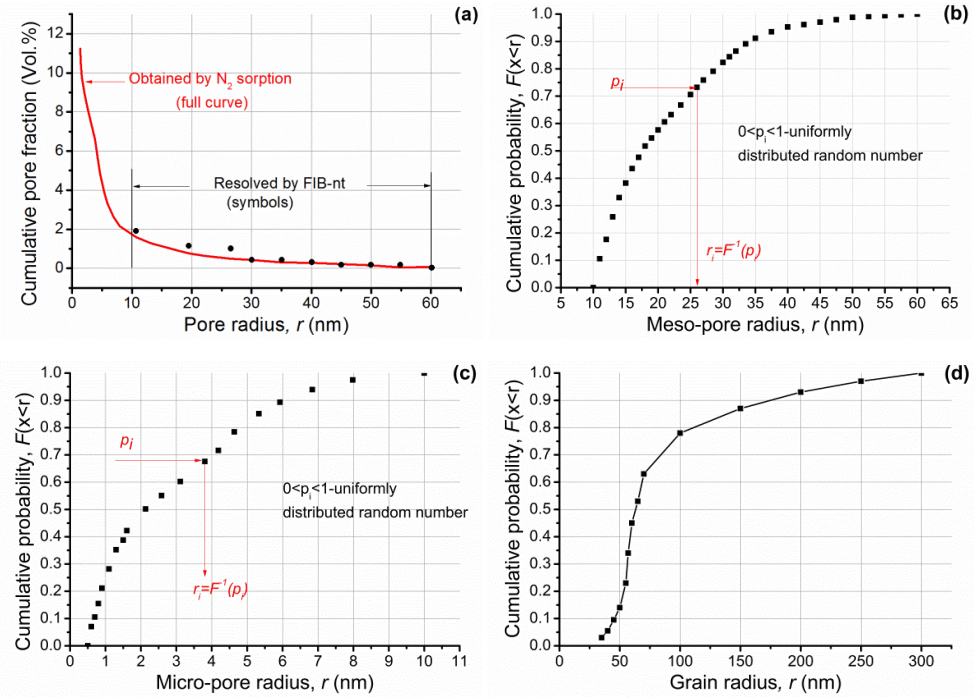

Fig. 3: Microstructure characteristics of OPA: (a) cumulative pore volume fraction versus pore size determined by FIB-nt and N_2 adsorption analyses [23]; (b) cumulative distribution of meso-pore sizes; (c) cumulative distribution of micro-pore sizes with assumed probability density from [18]; (d) cumulative distribution of carbonate grain sizes [24].

3 Transport modelling and data

3.1. Diffusion equation

The driving force for local diffusion is the concentration gradient between connected nodes with resistance provided by the pores. In reality, pores have different shapes. However, the experimental data of cumulative pore fraction from Keller *et al.* [23] substituted the irregular shape of pores by equivalent circular shape. To reflect realistic situation, circularity dependent on shape factor is introduced to consider the effect of pore shapes when all pores are assumed to be circular [38]. In our work, the pores are considered to be elongated conduits with different pore shapes. The diffusive flow, F_{ij} [kg/s], through a pore is described by the Fick's first law

$$F_{ij} = 4\pi G_{ij} D_{ij} A_{ij} \frac{c_i - c_j}{l_{ij}} \quad (4)$$

where D_{ij} [m^2/s] is the pore diffusivity, which is calculated in the same way as in Xiong *et al.* [1, 39], A_{ij} [m^2] is the pore cross-section area, l_{ij} [m] is the pore length, $c_i - c_j$ [kg/m^3] is the concentration difference between nodes, $4\pi G_{ij}$ [-] is the circularity.

To verify the pore network model, two diffusion species are considered in this work. One is HTO, a neutral solute with molecular size of r_A = 0.1 nm [18]. The other is a neutral U(VI) complex, $Ca_2UO_2(CO_3)_3$, which dominates the U(VI) speciation in OPA pore water at room temperature to nearly 100 % [40]. The molecular size of this complex is r_A = 0.524 nm [41]. These two species are selected for comparison with experimental data on their diffusivity in OPA. The free molecular diffusion coefficients calculated with the Einstein-Stokes equation at room temperature, are $D_0 = 2.24\times10^{-9}$ m^2/s for HTO [42] and $D_0 = 4.66\times10^{-10}$ m^2/s for U(VI) [43], respectively.

3.2. Flow equation

We assume saturated flow through the network. The flow field in the network is described by imposing two different pressures on two opposing boundaries of the network. The remaining boundaries of the network do not permit flow. For a pore with area A_{ij} [m^2] and shape factor G_{ij}, connecting nodes i and j, the volume flow rate of diffusing species, q_{ij} [m^3/s], is described by the Hagen-Poiseuille equation

$$q_{ij} = m\frac{A_{ij}^2 G_{ij}}{\mu l_{ij}}\left(p_i - p_j\right) \tag{5}$$

where m [-] is a pore-shape coefficient (for a circular, an equilateral and a square tube, m is 0.5, 0.6, and 0.5623, respectively [44]), μ [Pa·s] is the dynamic viscosity, p_i and p_j [Pa] are pressures at pore i and j, respectively. Eq. (5) is considered to be appropriate for describing flow in pores [45] and is valid for laminar flow in a wide range of Reynolds numbers. For incompressible, steady state flow, the sum of pore discharges at node must be zero

$$\sum_{j=1}^{z_i} q_{ij} = 0 \tag{6}$$

where z_i [-] is the number of pores connected to node i. Then the average pore water velocity through the pore network, $\bar{v}$ [m/s], can be determined as

$$\bar{v} = \frac{QL}{V} \tag{7}$$

where Q [m^3/s] is the total discharge through the network; L [m] is the network length in the flow direction; V [m^3] is the volume of the network.

3.3. Mass transport equation

The transient dynamics of a solute subject to sorption and transport are described by the following equations:

$$\frac{\partial c}{\partial t} = \left(\frac{\partial c}{\partial t}\right)_{adv} + \left(\frac{\partial c}{\partial t}\right)_{dif} + \left(\frac{\partial c}{\partial t}\right)_{sorp} \tag{8}$$

$$\left(\frac{\partial c}{\partial t}\right)_{adv} = -\nabla(cu) \tag{9}$$

$$\left(\frac{\partial c}{\partial t}\right)_{dif} = \nabla D(\nabla c) \tag{10}$$

$$L\left(\frac{\partial c}{\partial t}\right)_{sorp} = -\frac{\partial s}{\partial t} \tag{11}$$

where t [s] is time, c [kg/m^3] is the concentration of the species in the system, u [m/s] is the fluid velocity vector, D [m^2/s] is the diffusion coefficient, s is the adsorbed mass onto the solid phase [kg/m^2], and L is the throat length [m].

A temporal and spatial discretization of above equations is used to describe mass transport through a pore

$$V_{ij}\frac{dc_{ij}}{dt} = V_{ij}u_{ij}\frac{c_i - c_j}{l_{ij}} + F_{ij} - S_{ij}\frac{ds_{ij}}{dt}. \tag{12}$$

Substituting Eq. (4) and (5) into Eq. (12), the mass flow of species in a throat is

$$V_{ij}\frac{dc_{ij}}{dt} = q_{ij}(c_i - c_j) + 4\pi G_{ij}D_{ij}A_{ij}\frac{c_i - c_j}{l_{ij}} - S_{ij}\frac{ds_{ij}}{dt}, \tag{13}$$

where q_{ij} [m^3/s] is the volumetric flow within the throat, c_{ij} [kg/m^3] is the average concentration in the pore, s_{ij} [kg/m^2] is mass adsorbed per unit area of the pore wall, S_{ij} [m^2] is the surface area, V_{ij} [m^3] is the pore volume [46].

Linear equilibrium adsorption is described by:

$$s_{ij} = k_{a,ij}c_{ij}, \tag{14}$$

where $k_{a,ij}$ [m] is the distribution coefficient normalized to the surface area (k_d/S_{ij}) [47].

Then Eq. (13) becomes

$$V_{ij}\left(1+k_{a,ij}\beta\right)\frac{dc_{ij}}{dt}=q_{ij}(c_i-c_j)+4\pi G_{ij}D_{ij}A_{ij}\frac{c_i-c_j}{l_{ij}}, \quad (15)$$

where $\beta=S_{ij}/V_{ij}$ [1/m].

For nonlinear equilibrium adsorption the Freundlich isotherm [48] is used:

$$s_{ij}=ac_{ij}^{b}, \quad (16)$$

leading to

$$V_{ij}\left(1+a\beta c_{ij}^{b-1}\right)\frac{dc_{ij}}{dt}=q_{ij}(c_i-c_j)+4\pi G_{ij}D_{ij}A_{ij}\frac{c_i-c_j}{l_{ij}}, \quad (17)$$

where a [m^{3b-2}/kg^{b-1}] and b [-] (b>1) are coefficients for sorption.

3.4. Network transport analysis

The system illustrated in Fig. 2(b) is a 3D mathematical graph – sites are graph nodes, bonds are graph edges. The graph topological structure (connectivity) is described by the so-called incidence matrix $\underline{\mathbf{A}}$ of dimensions E × N, where E is the number of edges (pores) and N is the number of nodes (pore junctions). An element of this matrix, a_{en}, can be either -1, +1, or 0, if node n is the first, second or not incident of edge e.

The incidence matrix describes both the topological structure of the system, which can be used for connectivity analysis, and the derivative of a discrete function defined on the nodes [49]. Specifically, a concentration field on the graph nodes, vector $\underline{\mathbf{C}}$ of dimension N, has a gradient given by the matrix product $\underline{\mathbf{A}}\ \underline{\mathbf{C}}$, which is a discrete field on the edges, vector $\underline{\nabla\mathbf{C}}$ of dimension E. As importantly, the transpose of the incidence matrix describes the derivative of a discrete function defined on the edges. Specifically, a mass flow field on the graph edges, a vector $\underline{\mathbf{J}}$ of dimension E, has a gradient given by $\underline{\mathbf{A}}^{\mathbf{T}}\ \underline{\mathbf{J}}$, which is a discrete field on the nodes, a vector $\underline{\nabla\mathbf{J}}$ of dimension N.

The components of the discrete field of edge flows, $\underline{\mathbf{J}}$, are calculated by Eq. (15) or Eq. (17), i.e. each component is the edge gradient scaled by an edge weight given by $W_e = (q_{ij}+D_{ij}\,A_{ij}\,/\,L_{ij})/(1+k_a\beta)$ or $W_e = (q_{ij}+D_{ij}\,A_{ij}\,/\,L_{ij})/(1+ac_{ij}^{b-1}\beta)$ for linear and nonlinear sorption at pore scale, respectively. Clearly, the edge weight depends on the assigned pore radius, velocity in the pore, selected length scale, radius of diffusing species, and sorption coefficient. For convenience the edge weights are arranged in a diagonal matrix, $\underline{\mathbf{W}}$, of dimensions E × E,

where the element in row and column e is the weight of edge e. Thus, the discrete flow field is given by $\underline{\mathbf{J}} = -\underline{\underline{\mathbf{W}}}\,\underline{\mathbf{A}}\,\underline{\mathbf{C}}$.

The mass transport through the graph is governed by mass conservation at nodes, i.e. the rate of change of diffusing species mass at the nodes equals the resultant mass flows through the nodes. The latter is the algebraic sum of the flows through adjacent edges, which is the divergence of the flow field given by $\underline{\mathbf{A}}^{\mathrm{T}}\underline{\mathbf{J}}$. Thus, the process of mass transport through a weighted graph is formulated mathematically by

$$V_n \frac{d\underline{\mathbf{C}}}{dt} = -\underline{\underline{\mathbf{A}}}^{\mathrm{T}}\,\underline{\underline{\mathbf{W}}}\,\underline{\underline{\mathbf{A}}}\,\underline{\mathbf{C}}, \tag{18}$$

where V_n is the node volume, which can be taken as cell volume, t is the time. This must be supplemented by initial and boundary conditions, similarly to continuum problems, but now defined on a discrete set of nodes. It is sufficient to point out that the matrix system of Eq. (18), supplemented by initial concentrations at all nodes and prescribed concentrations or fluxes at boundary nodes, is solved numerically to find nodal concentrations and boundary fluxes at any future time. The simulations terminate when steady-state is reached, i.e. when concentrations at all nodes are constant.

The formulation of flow via discrete analysis on graphs is highly beneficial for incorporating system evolution compared to traditional finite element or finite difference formulations. Conceptually, it shows the intrinsic relation between the pore space topological structure and transport, both described via the incidence matrix. Practically, it differentiates clearly between effects of connectivity, captured by the incidence matrix $\underline{\mathbf{A}}$, and geometry and physics, captured by the edge weight matrix $\underline{\underline{\mathbf{W}}}$. This facilitates the incorporation of potential pore space changing mechanisms in a computationally effective way. For example, local pore geometrical changes arising from corrosion, sorption, bacterial film growth, deformation, etc., will affect corresponding coefficients of $\underline{\underline{\mathbf{W}}}$ only but leave $\underline{\mathbf{A}}$ constant. Material failures, such as micro-cracks, during evolution present a more complex case. These change the connectivity, i.e. they alter $\underline{\mathbf{A}}$, and introduce geometry and physics for the new edges, i.e. modify $\underline{\underline{\mathbf{W}}}$.

Immutable pore systems have been analysed for the calculation of macroscopic diffusivity. Comparing the calculated results with experimental diffusion coefficients reported in the literature, the realism of the model construction in terms of initial pore space geometry and

topology will be verified. In this work, the effects of pore shapes, sorption coefficient, and velocities are analysed based on previous work.

3.5. Diffusion experiments

OPA bore core samples from the Mont Terri rock laboratory in Switzerland were used in all diffusion experiments applying the experimental set-up described in Van Loon *et al.* [50] and shown in Fig. 4. The samples (thickness: 11 mm, diameter: 25.5 mm) were placed in stainless steel diffusion cells between two stainless steel filter plates (316L, pore diameter: 0.01 mm; MOTT industrial division, Farmington, USA). Synthetic OPA pore water [51] was used as background electrolyte in all diffusion experiments. Each diffusion cell was coupled with a peristaltic pump (mod. Ecoline, Ismatec, IDEX Health & Science, Glattbrugg, Switzerland) and a source and receiving reservoir filled with 200 mL and 20 mL synthetic OPA pore water, respectively. The solutions were circulating through the end plates of the cells in order to saturate the samples. The saturation time amounted to three weeks. Subsequently, the solutions were replaced by fresh ones, whereby the source reservoir contained the tracer and thus, tracer diffusion perpendicular to the clay bedding was started.

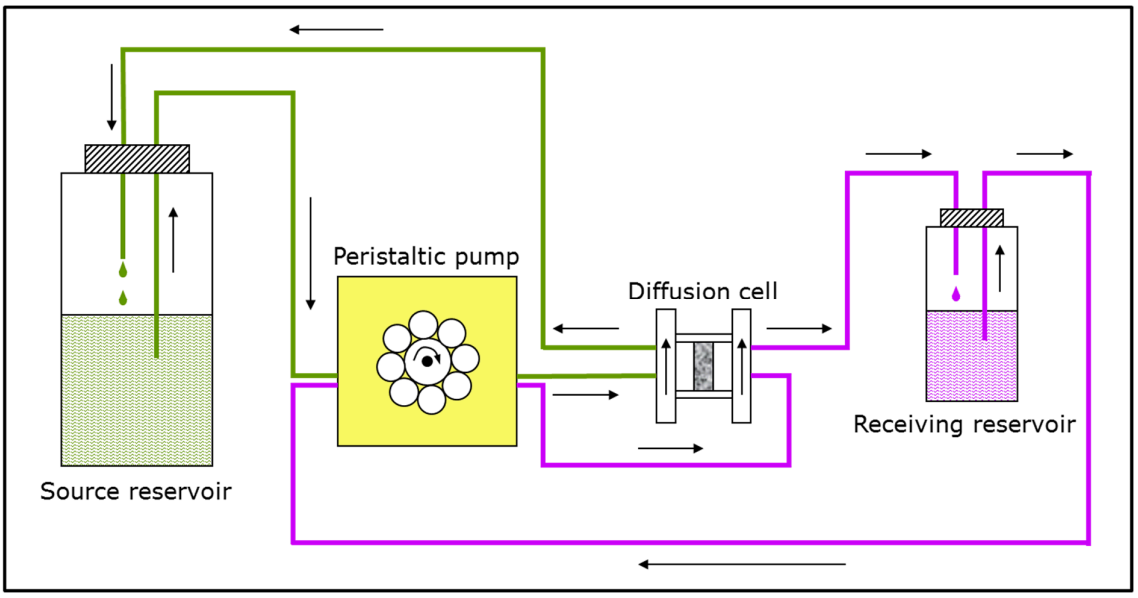

Fig. 4: Schematic depiction of the experimental set-up used in the diffusion experiments (based on Van Loon *et al.* [50]).

At first, HTO through- and out-diffusion experiments were performed according to the procedure described by Van Loon *et al.* [50] in order to determine values for the total porosity (θ) of the clay samples (c_0(HTO) = 1000 Bq/mL). After that, the U(VI) in-diffusion

491 was studied ($c_0(^{233}U(VI)) = 1\times10^{-6}$ mol/L). After 3 months, the diffusion experiments were
492 stopped and the clay samples were removed from the cells. With the help of the abrasive
493 peeling technique [52], U(VI) diffusion profiles were determined. The peeled layers were
494 extracted for U(VI) content by 1 mol/L HNO_3 (*p.a.*, Roth, Karlsruhe, Germany). The tracer
495 concentrations in the extracts were determined by liquid scintillation counting (mod. TriCarb
496 3100 TR, Perkin Elmer, Freiburg, Germany). All experimental results were evaluated using
497 the commercial software COMSOL Multiphysics: Finite-element software package 3.5a
498 (2008) and 4.2a (2011). A detailed description of all diffusion experiments can be found in
499 Joseph *et al.* [25, 27].
500
501
502
503

4 Results and discussion

4.1. Boundary value problems on graphs

With respect to a coordinate system (X_1, X_2, X_3) normal to the square faces of the unit cell (see Fig. 1), a pore network skeleton within the boxed region ($0 \le X_1 \le N \cdot S_1$, $0 \le X_2 \le N \cdot S_2$, $0 \le X_3 \le N \cdot S_3$) was used. Here, S_1, S_2, S_3, are the cell sizes in the three coordinate directions and N is the number of cells in each coordinate direction. Pore networks were built on skeletons with increasing N using the process from sub-sections 2.1-2.4. Statistically representative distribution of pore sizes was obtained with relatively small number of cells, e.g., it was sufficient that $N > 5$ for the distributed pores to follow the experimental pore size distribution closely. Further, the effect of the random spatial allocation of pores on results was analysed using 10 different realisations for each N. It was found that for $N = 20$, the variation of results from the average was reduced to under 10%. This was judged to be an acceptable accuracy and the diffusivity results reported hereafter were obtained as the average values from 10 realisations on a skeleton with $N = 20$. This skeleton contains *Nodes* = 110860 nodes, i.e. potential pore junctions, and *Edges* = 533520 bonds, i.e. potential pore locations.

Zero concentration of diffusing species is taken as initial conditions in all nodes. The boundary conditions reflect a particular experimental setup, where concentrations c_0 and c_1, are prescribed on two opposite boundaries, while the remaining four boundaries do not permit flux. The selection of the two boundaries depends on the macroscopic transport properties being analysed. Specifically, the boundary conditions used to calculate the macroscopic transport properties parallel to bedding direction (1, 0, 0), D_1, are: prescribed concentration c_0, in all nodes on plane $X_1 = 0$; prescribed concentration c_1 in all nodes on plane $X_1 = 20S_1$; zero flux through all nodes on planes $X_2 = 0$, $X_2 = 20S_2$, $X_3 = 0$, $X_3 = 20S_3$. For calculating the macroscopic transport properties perpendicular to the bedding direction, say (0, 1, 0), D_2, the boundary conditions are: prescribed concentration c_0 in all nodes on plane $X_2 = 0$; prescribed concentration c_1 in all nodes on plane $X_2 = 20S_2$; zero flux through all nodes on planes $X_1 = 0$, $X_1 = 20S_1$, $X_3 = 0$, $X_3 = 20S_3$.

One example of diffusion in the bedding direction for a system with unequal length parameters and circular cross sectional pores is shown in Fig. 5 by the solute concentration profiles at select times. The prescribed concentration c_0 on plane X_1 is 1 mol/m^3 and the

prescribed concentration c_1 on plane X_0 is 0. These are snapshots taken from the whole history obtained by numerical simulation based on Eq. (4). The profiles are shown on the cellular assembly, rather than on the graph representing the pore network, for clarity.

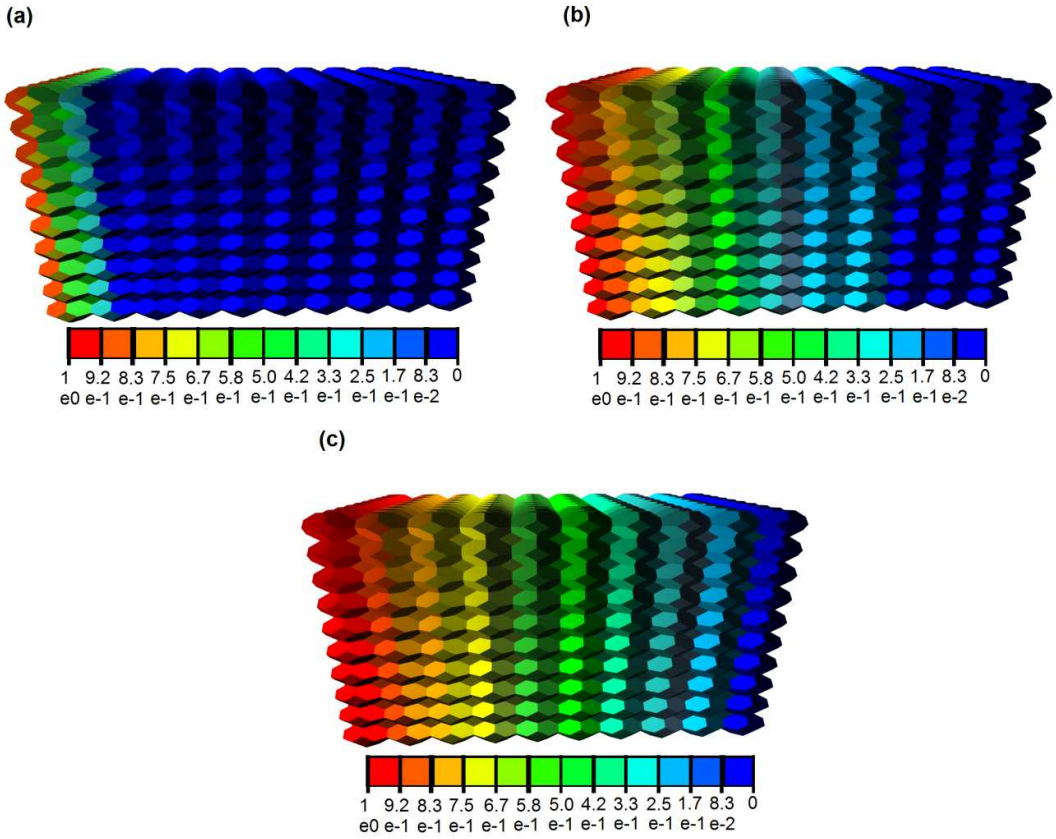

Fig. 5: Concentration profiles of HTO [mol/m^3] at time t = 0.1 s (a), t = 0.5 s (b), and t = 1 s (c). The pores are assumed with circular cross section.

4.2. Effective diffusivity

The constructed pore networks exhibit macroscopic tortuosity (path lengthening), introduced by the selection of transport pathways along the interfaces between solid phases regions. This tortuosity depends on the material texture, represented here by the ratios of the cell length parameters in three perpendicular directions. Experimental results show that tortuosity is smaller in the bedding direction [26]. Therefore, we investigate the effect of larger cell length in the bedding direction and smaller cell lengths in the directions perpendicular to bedding. The results of different cell length ratios have been discussed in a previous paper [39]. It was shown that the calculated effective diffusivity considering both carbonates and quartz as

554 particles is closest to the experimental value when the ratio of the cell length parameters is: S_1
555 / S_2 = 2 and the out-of-bedding directions are not differentiated, i.e. $S_2 = S_3$ is assumed. In this
556 work, the same ratio of the cell length parameters and volume percentage of particles are
557 adopted. For cellular assembly of this given ratio, 10 realisations of pore spatial distributions
558 were analysed to obtain the transport in the bedding, S_1, and out-of-bedding, S_2, directions.
559 The results reported are the averaged values of these analyses.
560
561 The diffusion of tracer molecules in clay has shown that mainly neutral and cationic species
562 diffuse in the interlayer water, diffuse layer water and the free pore water [53]. Experiments
563 reported that the accessible porosity for HTO [25, 26, 37, 54] agrees very well with total
564 porosity in OPA [22], which implies that almost all the pores in OPA are available. The total
565 porosity has been used to simulate the effective diffusion coefficients of HTO in this work. In
566 Fig. 6, the effective diffusivities of HTO and U(VI) parallel and perpendicular to the bedding,
567 D_1 and D_2, are shown to increase as the average shape factor G increases. The calculated
568 effective diffusivity of HTO is in the following ranges: $D_1 = 5.41\times10^{-11} \sim 17.10\times10^{-11}$ m^2/s;
569 $D_2 = 1.58\times10^{-11} \sim 5.03\times10^{-11}$ m^2/s (see Fig. 6a). Reported experimentally obtained values for
570 HTO diffusion in OPA shown in Fig. 6a are in the range of $D_1 = (5.4\pm0.4)\times10^{-11}$ m^2/s [26]
571 and $D_2 = (1.48\pm0.03)\times10^{-11}$ m^2/s [25], $(1.26\pm0.09)\times10^{-11}$ m^2/s [25], $(1.23\pm0.06)\times10^{-11}$ m^2/s
572 [26], $(1.67\pm0.12)\times10^{-11}$ m^2/s [27], $(1.33\pm0.11)\times10^{-11}$ m^2/s [27] determined for different bore
573 core samples. In OPA, the accessible porosity is different for the various species resulting in
574 different effective diffusivities. The increased diffusion of cations is explained either by
575 interlayer or by diffusion in the electrical double layer [37, 55] that surrounds the negatively
576 charged clay surface and contains an excess of cations [54, 56-61]. The diminished diffusion
577 of anions is due to their limited access to the interlayer space. This is caused by the overlay of
578 double layers. As a result the electric potential becomes considerably large [62].
579
580 If in the model the diffusing U(VI) species is neutral, then the same initial accessible porosity
581 as for HTO can be assumed. The simulated effective diffusivity of U(VI) in the bedding
582 direction, D_1, (cf. Fig. 6b) is in the range of $8.04\times10^{-12} \sim 2.56\times10^{-11}$ m^2/s, and in the
583 perpendicular direction, D_2, is from 1.98×10^{-12} to 7.26×10^{-12} m^2/s. Experimental data for
584 U(VI) in the perpendicular direction are $1.5\times10^{-12} \sim 2.3\times10^{-12}$ m^2/s [25, 27]. The simulated
585 results for HTO and U(VI) are in good agreement with experimental investigations when
586 average shape factor, G, is equal to 0.025 (cf. Fig. 6). In OPA, three types of water accessible
587 for diffusion can be distinguished. The solute, for instance a U(VI) species, enters freely the

larger pores, since it resides in an electrically neutral solution, the so-called free pore-water. On the net negatively charged clay surface, the water turns into a diffuse double layer. The charge deficiency can be balanced by exchangeable cations, anions are repulsed from the surface. The third type is interlayer water in the smectite fraction of OPA. It is considered to contain exchangeable cations only, which behave chemically and physically comparable to the surface complexed cations. The types of water or pore space accessible for diffusion depends on the diffusing species [22, 37, 63, 64]. Specifically, diffusion of cations is enhanced, and that of anions diminished, relative to a neutral tracer such as HTO [37]. The here discussed effective diffusivity excludes sorption effects of the U(VI) species, $Ca_2UO_2(CO_3)_3(aq)$, on OPA during their migration, only the pure transport process is considered. Since the same approach was used for modelling HTO and U(VI) diffusion except that the radius of the diffusing species was changed, the observed difference of one order of magnitude in D_2 for HTO and U(VI) can be attributed solely to size exclusion effects and not to charge effects of attracted or repulsed charged U(VI) species. It has been demonstrated in previous works [54, 65], that the amount of electrical double layer water is approximately equal to half of the porosity. This means that anions cannot access almost half of the porosity, manifested in anion exclusion effect on diffusivity. Hence, the effective diffusivity of $UO_2(CO_3)_3^{4-}$ and U(VI) species should be different despite of their similar molecular sizes. Therefore, it can be concluded that the neutral $Ca_2UO_2(CO_3)_3(aq)$ complex is not only the dominant U(VI) species in the OPA pore water solution in the source reservoir but also the main diffusing U(VI) species through OPA.

Overall, the model in this work can predict diffusion in OPA very well. The difference between the computational and the experimental results could be partially due to a difference between the microstructure characteristics of OPA obtained by Keller *et al.* [23, 24] used for model construction, and the clays used for experimental measurement of effective diffusion coefficients by Van Loon *et al.* [26] and Joseph *et al.* [25, 27].

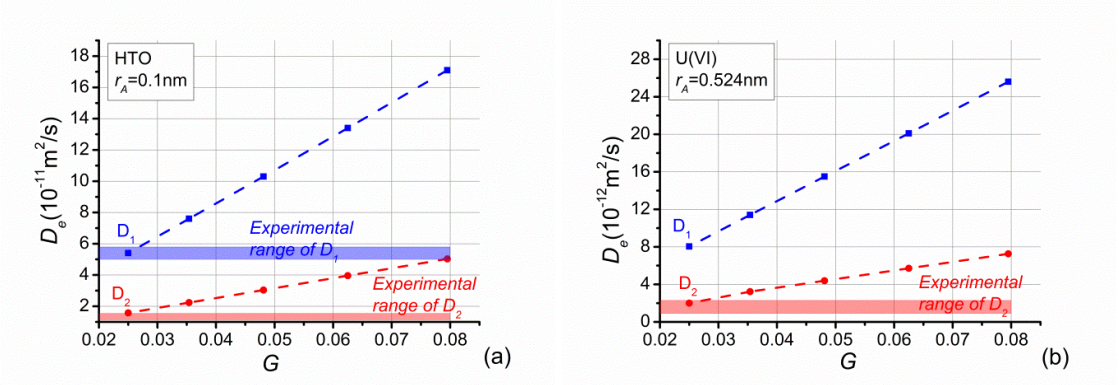

Fig. 6: Calculated effective diffusivity of HTO (a) and U(VI) (b) in OPA as a function of shape factor and accounting for carbonates and quartz as non-porous particles with combined volume fraction of 0.35. Experimentally determined ranges of OPA effective diffusion coefficients are shown for comparison.

4.3. Apparent diffusivity

To investigate the effects of the shape factor on sorption, apparent diffusivities of U(VI) with different average shape factors are analysed and presented in Fig. 7(a). It is obvious that the increase of the average shape factor in the system yields an increase of apparent diffusivities of U(VI) in both directions investigated. Because the shape factor is the ratio between cross section area and perimeter, smaller shape factors lead to smaller ratios between pore volume and surface area. The larger the surface area the more species adsorb onto the pore wall. The variation of U(VI) apparent diffusivities is bigger than the growth of U(VI) effective diffusivities when the average shape factor increases from 0.025 to 0.08. In addition, the change of apparent diffusivities in the bedding direction is larger than apparent diffusivities perpendicular to the bedding plane. This is due to the fact that elongated pores are distributed in the bedding direction. The shape factor only affects cross sectional shape.

Because effective diffusivities of U(VI) agree well with experimental values when the average shape factor, G, equals to 0.025, this value of G is adopted to study sorption effects of U(VI) in OPA. We assumed that linear sorption occurs at pore-scale according to experimental investigation [35]. Apparent diffusivities of U(VI) species are shown in Fig. 7(b) as a function of distribution coefficients, k_a. It is clear that the increase of k_a yields reductions of the apparent diffusivity, D_{1a} and D_{2a}. Because the adsorbed mass is dependent on the value of k_a, more species will be adsorbed when k_a increases. As a consequence, migration of the U(VI) species retards because of their stronger interaction with the OPA pore walls. In

addition, since more species are adsorbed onto the pore-wall, the cross section of pores allowed for diffusion becomes smaller and thus the accessible pore space will be reduced. Notably, the decrease of the apparent diffusivity becomes slowly as the adsorption coefficient increases. This is an illustration of the non-linear effect of the sorption in the system.

The calculated results of apparent diffusivities are in the following ranges: $D_{1a} = 8.35\times10^{-14} \sim 2.05\times10^{-13}$ m^2/s; $D_{2a} = 1.98\times10^{-14} \sim 4.87\times10^{-14}$ m^2/s, see Fig. 7(b), when k_a decreases from 250 nm to 100 nm. Reported experimentally obtained values for U(VI) complexes diffusion in OPA are $D_{1a} = 9.5\times10^{-14}$ m^2/s [28], $D_{2a} = 2.8\times10^{-14} \sim 3.4\times10^{-14}$ m^2/s [25, 27], 2.8×10^{-14} m^2/s [28]. These ranges are given in Fig. 7(b). Direct comparison shows that the simulation and the experimental results are in reasonable agreement when k_a is about 200 nm. The experimental distribution coefficients k_d measured by experiments were parallel to the bedding: 0.0142 m^3/kg [28], perpendicular to the bedding: 0.025±0.003 m^3/kg [25], 0.038±0.005 m^3/kg [27], 0.0138 m^3/kg [28]. Since k_a is the distribution coefficient, k_d, normalised by surface area, and the surface area obtained by ethylene glycol monoethyl ether for OPA varies from 80 to 107 m^2/g (the average value is 94 m^2/g) [22], the experimental k_a values range from 128 nm to 350 nm. This is very close to the simulated value of k_a. The sorption of U(VI) species is therefore linear.

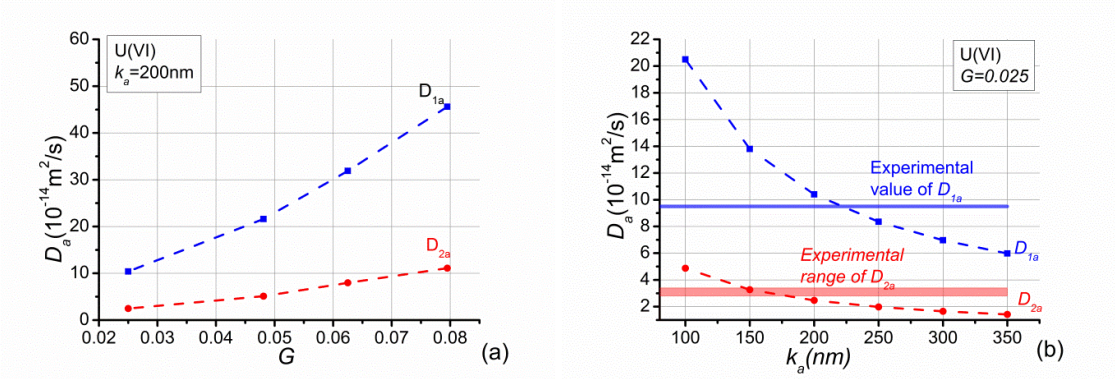

Fig. 7. Simulated apparent diffusivity of U(VI) in OPA. (a) the dependence on shape factor when distribution coefficient, k_a, equals 200 nm; (b) as a function of k_a, when $G = 0.025$, experimentally determined ranges of D_a values are shown for comparison.

The pore-scale Freundlich isotherm sorption, $s = ac^b$ (cf. Eq. (16)), is also studied in this work. Since this sorption equation is dependent on the pore-local concentration variation of solutes, the concentration applied at the boundaries must be clarified. This is different for the analysis of effective diffusion and linear sorption where the results are independent of the

prescribed concentration difference on the boundaries. We apply $C_0 = 0.05$ mol/m^3 at $X_0 = 0$, $C_1 = 0$ at $X_1 = 20S_1$, and no flux at other boundaries. The effects of parameters a and b on the apparent diffusivities are shown in Fig. 8. In Fig. 8(a), the increase of a yields a reduction of the apparent diffusivities of U(VI) in both directions when $b = 1.5$. The changes are similar with the situation of linear sorption, $s = k_a c$. In Fig. 8(b), the apparent diffusivities of U(VI) in both directions increase as b increase. The increase of apparent diffusivities becomes slowly with increasing b. This is due to the fact that the adsorbed mass becomes less as the parameter of b increases. The maximum values of apparent diffusivities will be very close to their effective diffusivities when b increases.

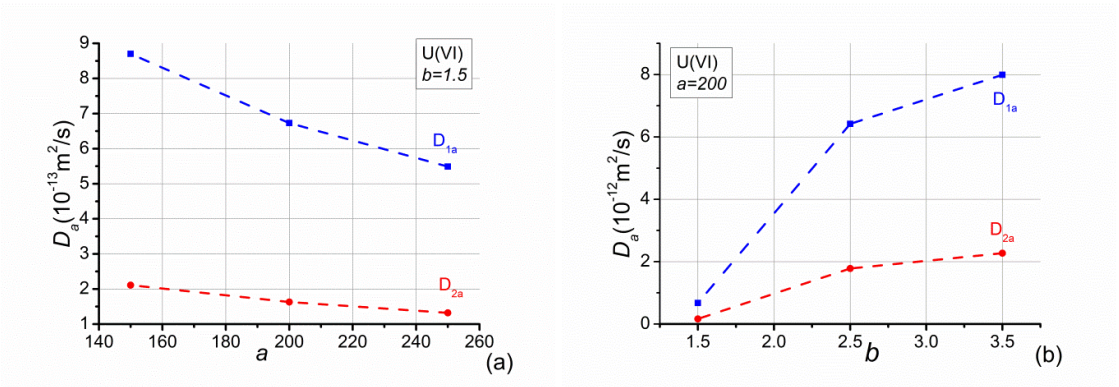

Fig. 8: Simulated apparent diffusivity of U(VI) in OPA by assuming a nonlinear sorption. Data are presented as a function of the Freundlich coefficient a (a) and the Freundlich exponent b (b). The shape factor equals to 0.025.

4.4. Velocity effect on transport property

Although hydraulic conductivity is very slow in OPA, it may be crucial for mass transport in other porous media. To illustrate the mechanism of diffusion-sorption-convection in porous media, we still use OPA as an example. The effect of velocity on transport of uranium species is considered. The shape factor is 0.025 and the distribution coefficient k_a is 200 nm. The evolution of uranium concentration at the outlet surface with time for different velocities is described in Fig. 9. Obviously, convection accelerates transport of species through the pore network model. The larger the velocity through the pore network model, the faster the species arrive the outlet surface. There is not much variation in the time evolution of the outlet concentration when velocity increases from 0 to 0.186 mm/s. This is in agreement with the fact that not convection but molecular diffusion is the main transport mechanism for radionuclides in OPA.

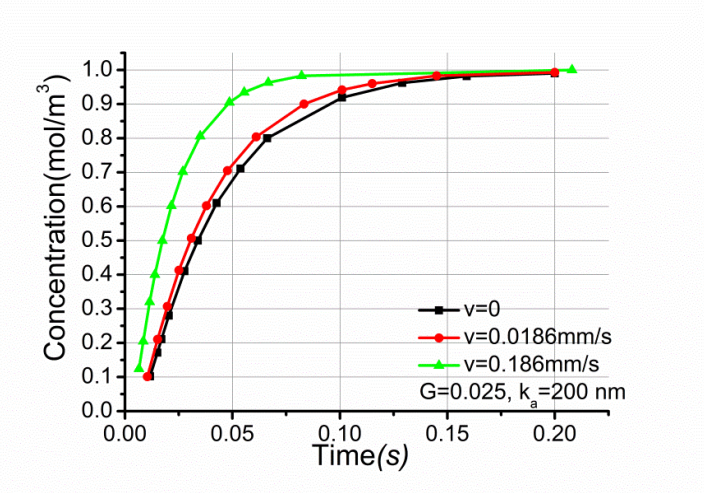

Fig. 9: Time history of uranium concentration at the outlet surface for different velocities, the distribution coefficient k_a is 200 nm, the pore shape factor is 0.025.

5 Conclusions

A discrete model for mass transport through porous media has been proposed to balance incomplete knowledge of geometrical and topological pore system characteristics.

The effect of clay's texture on the transport properties has been investigated by analysing the transport of HTO and U(VI) through OPA. The anisotropy and heterogeneity of the clay can be simulated via different length parameters and percentage of pores in different directions. Different pore shapes are also taken into account in this model, which is very important for multi-phase transport. Calculated diffusion coefficients are within the ranges of experimental data. The results suggest that U(VI) diffuses as neutral species, $Ca_2UO_2(CO_3)_3(aq)$, through OPA. Because only species in the source reservoir solution are known in experiments, the methodology proposed in this work could clarify the kind of U(VI) species (anion, cation or neutral species) diffusing in OPA. In addition, the idea has been extended to account for sorption and convection. Physical sorption is simulated in each pore, which is more accurate and realistic compared to previous coarse grained mathematical formula by changing pore radii [1].

Although this work has used a particular material to illustrate the methodology and its application, the model is suitable for modelling and simulation of other micro- and meso-porous materials. The methodology proposed in this work can be used to study sorption of

722 species that may not be easily studied by classical in-diffusion or through-diffusion methods,
723 for example, when the species is adsorbed onto laboratory materials (e.g., cells, vessels, and
724 tubing).
725
726 The proposed model can be potentially used for coupling with deformation and fracture of
727 porous media, where the pore system and the solid phase, represented as dual graphs, will
728 interact effectively. Models mimicking the coupling are possible and are subject of ongoing
729 work. For example, our immediate plans are to study the effect of micro-cracking due to
730 thermo-mechanical loads on the diffusion with application to long-term behaviour of OPA in
731 a nuclear wastes repository. The goal with the concept development is to have a set of
732 discrete models, i.e. PNM accounting for transport mechanism and lattice models of the solid
733 phase developed for analysis of damage evolution via micro-cracking [19], that evolve
734 concurrently at their own rates and inform each other about changes in their structures. Such
735 a coupled problem could be of great interest in many disciplines, e.g., shale gas extraction,
736 dams, and underground cavities in hydropower engineering. In these applications, the
737 evolution of permeability rather than diffusivity of the medium is required, but the
738 methodology developed in this work would be the same.
739

740 ## Acknowledgements

741 Q. Xiong acknowledges gratefully the Doctoral Award from the President of The University
742 of Manchester. A. Jivkov acknowledges the support from BNFL for the Research Centre for
743 Radwaste & Decommissioning and from EdF R&D for the Modelling & Simulation Centre.
744 C. Joseph and K. Schmeide thank the German Federal Ministry for Economic Affairs and
745 Energy (BMWi) for financial support (no. 02 E 10971).

746 This work was performed under the auspices of the U.S. Department of Energy by Lawrence
747 Livermore National Laboratory under Contract DE-AC52-07NA27344.
748

749 ## References

750 [1] Xiong Q, Jivkov AP, Yates JR. Discrete modelling of contaminant diffusion in porous
751 media with sorption. Microporous and Mesoporous Materials. 2014;185:51-60.
752 [2] Blunt MJ, Bijeljic B, Dong H, Gharbi O, Iglauer S, Mostaghimi P, Paluszny A,
753 Pentland C. Pore-scale imaging and modelling. Advances in Water Resources. 2013;51:197-
754 216.
755 [3] Tang L. Chloride transport in concrete-measurement and prediction. 1996.

[4] Ezeuko C, Sen A, Grigoryan A, Gates I. Pore - network modeling of biofilm evolution in porous media. Biotechnology and Bioengineering. 2011;108(10):2413-2423.

[5] Whitaker S. Diffusion and dispersion in porous media. AIChE Journal. 1967;13(3):420-427.

[6] White AF, Brantley SL. The effect of time on the weathering of silicate minerals: why do weathering rates differ in the laboratory and field? Chemical Geology. 2003;202(3–4):479-506.

[7] Köhne JM, Schlüter S, Vogel H-J. Predicting solute transport in structured soil using pore network models. Vadose Zone Journal. 2011;10(3):1082-1096.

[8] Blunt MJ. Flow in porous media—pore-network models and multiphase flow. Current Opinion in Colloid & Interface Science. 2001;6(3):197-207.

[9] Blunt MJ, Jackson MD, Piri M, Valvatne PH. Detailed physics, predictive capabilities and macroscopic consequences for pore-network models of multiphase flow. Advances in Water Resources. 2002;25(8):1069-1089.

[10] Berkowitz B, Ewing RP. Percolation theory and network modeling applications in soil physics. Surveys in Geophysics. 1998;19(1):23-72.

[11] Wilkinson D, Willemsen JF. Invasion percolation: a new form of percolation theory. Journal of Physics A: Mathematical and General. 1983;16(14):3365.

[12] Meyers J, Crosser O, Liapis AI. Pore network modelling: determination of the dynamic profiles of the pore diffusivity and its effect on column performance as the loading of the solute in the adsorbed phase varies with time. Journal of Chromatography A. 2001;908(1):35-47.

[13] Jivkov AP, Hollis C, Etiese F, McDonald SA, Withers PJ. A novel architecture for pore network modelling with applications to permeability of porous media. Journal of Hydrology. 2013;486:246-258.

[14] Gao S, Meegoda JN, Hu L. Two methods for pore network of porous media. International Journal for Numerical and Analytical Methods in Geomechanics. 2012;36(18):1954-1970.

[15] Al-Raoush R, Willson C. Extraction of physically realistic pore network properties from three-dimensional synchrotron X-ray microtomography images of unconsolidated porous media systems. Journal of Hydrology. 2005;300(1):44-64.

[16] Dong H, Blunt M. Pore-network extraction from micro-computerized-tomography images. Physical Review E. 2009;80(3).

[17] Piri M, Blunt MJ. Three-dimensional mixed-wet random pore-scale network modeling of two-and three-phase flow in porous media. II. Results. Physical Review E. 2005;71(2):026302.

[18] Jivkov AP, Xiong Q. A Network Model for Diffusion in Media with Partially Resolvable Pore Space Characteristics. Transport in Porous Media. 2014;105(1):83-104.

[19] Jivkov AP, Gunther M, Travis KP. Site-bond modelling of porous quasi-brittle media. Mineralogical Magazine. 2012;76(8):2969-2974.

[20] Jivkov AP, Yates JR. Elastic behaviour of a regular lattice for meso-scale modelling of solids. International Journal of Solids and Structures. 2012;49(22):3089-3099.

[21] Jivkov AP, Engelberg DL, Stein R, Petkovski M. Pore space and brittle damage evolution in concrete. Engineering Fracture Mechanics. 2013;110:378-395.

[22] NAGRA. Projekt Opalinuston: Synthese der geowissenschaftlichen Untersuchungsergebnisse Technischer Bericht 2002;02 -03:250-252.

[23] Keller LM, Holzer L, Wepf R, Gasser P. 3D geometry and topology of pore pathways in Opalinus clay: Implications for mass transport. Appl Clay Sci. 2011;52(1-2):85-95.

804 [24] Keller LM, Schuetz P, Erni R, Rossell MD, Lucas F, Gasser P, Holzer L.
805 Characterization of multi-scale microstructural features in Opalinus Clay. Microporous and
806 Mesoporous Materials. 2013;170:83-94.

807 [25] Joseph C, Van Loon LR, Jakob A, Steudtner R, Schmeide K, Sachs S, Bernhard G.
808 Diffusion of U(VI) in Opalinus Clay: Influence of temperature and humic acid. Geochimica
809 et Cosmochimica Acta. 2013;109:74-89.

810 [26] Van Loon LR, Soler JM, Müller W, Bradbury MH. Anisotropic diffusion in layered
811 argillaceous rocks: a case study with Opalinus Clay. Environmental Science & Technology.
812 2004;38(21):5721-5728.

813 [27] Joseph C, Fritsch K, Steudtner R, Schmeide K. U(VI)-Sorption und -Diffusion an/in
814 Tonmineralen und Opalinuston – Einfluss von pH, Ionenstärke und Organika. 3 Workshop
815 des BMWi-Verbundvorhabens: Rückhaltung endlagerrelevanter Radionuklide im natürlichen
816 Tongestein und in salinaren Systemen. München; 2012.

817 [28] García-Gutiérrez M, Alonso U, Missana T, Cormenzana JL, Mingarro M, Morejón J,
818 Gil P. Diffusion Experiments with Opalinus and Callovo-Oxfordian Clays: Laboratory,
819 Large-Scale Experiments and Microscale Analysis by RBS. in: CIEMAT (Ed), Informes
820 Técnicos Ciemat 1168 Departamento de Medio Ambiente, Madrid. 2009.

821 [29] Kumar S, Kurtz SK, Banavar JR, Sharma M. Properties of a three-dimensional
822 Poisson-Voronoi tesselation: A Monte Carlo study. Journal of Statistical Physics. 1992;67(3-
823 4):523-551.

824 [30] Wang X, Yang Z, Yates JR, Jivkov AP, Zhang C. Monte Carlo simulations of
825 mesoscale fracture modelling of concrete with random aggregates and pores. Construction
826 and Building Materials. 2015;75(0):35-45.

827 [31] Wang X, Yang Z, Jivkov AP. Monte Carlo simulations of mesoscale fracture of
828 concrete with random aggregates and pores: a size effect study. Construction and Building
829 Materials. 2015;80(0):262-272.

830 [32] Zhang M, Jivkov A. Microstructure-informed modelling of damage evolution in
831 cement paste using a site-bond model. Construction and Building Materials. 2014;66:731-742.

832 [33] Zhou D, Dillard LA, Blunt MJ. A physically based model of dissolution of
833 nonaqueous phase liquids in the saturated zone. Transport in Porous Media. 2000;39(2):227-
834 255.

835 [34] Mason G, Morrow NR. Capillary behavior of a perfectly wetting liquid in irregular
836 triangular tubes. Journal of Colloid and Interface Science. 1991;141(1):262-274.

837 [35] Wenk H-R, Voltolini M, Mazurek M, Van Loon L, Vinsot A. Preferred orientations
838 and anisotropy in shales: Callovo-Oxfordian shale (France) and Opalinus Clay (Switzerland).
839 Clays and Clay Minerals. 2008;56(3):285-306.

840 [36] Mazurek M, Gautschi A, Marschall P, Vigneron G, Lebon P, Delay J. Transferability
841 of geoscientific information from various sources (study sites, underground rock laboratories,
842 natural analogues) to support safety cases for radioactive waste repositories in argillaceous
843 formations. Physics and Chemistry of the Earth, Parts A/B/C. 2008;33, Supplement 1(0):S95-
844 S105.

845 [37] Appelo C, Van Loon L, Wersin P. Multicomponent diffusion of a suite of tracers
846 (HTO, Cl, Br, I, Na, Sr, Cs) in a single sample of Opalinus Clay. Geochimica et
847 Cosmochimica Acta. 2010;74(4):1201-1219.

848 [38] Houben ME, Desbois G, Urai JL. Pore morphology and distribution in the Shaly
849 facies of Opalinus Clay (Mont Terri, Switzerland): Insights from representative 2D BIB–
850 SEM investigations on mm to nm scale. Applied Clay Science. 2013;71:82-97.

851 [39] Xiong Q, Jivkov AP. Analysis of pore structure effects on diffusive transport in
852 Opalinus clay via pore network models. Mineralogical Magazine. 2015;accepted.

[40] Joseph C, Schmeide K, Sachs S, Brendler V, Geipel G, Bernhard G. Sorption of uranium(VI) onto Opalinus Clay in the absence and presence of humic acid in Opalinus Clay pore water. Chemical Geology. 2011;284(3–4):240-250.

[41] Bai J, Liu C, Ball WP. Study of sorption-retarded U (VI) diffusion in Hanford silt/clay material. Environmental Science & Technology. 2009;43(20):7706-7711.

[42] MontTerriProject. Long-term Diffusion (DI-A) Experiment: DI-A2: Diffusion of HTO, Br^-, I^-, Cs^+, $^{85}Sr^{2+}$ and $^{60}Co^{2+}$: Field activities, data and modelling. Report TR. 2010:2009-2004.

[43] Cappelezzo M, Capellari C, Pezzin S, Coelho L. Stokes-Einstein relation for pure simple fluids. The Journal of Chemical Physics. 2007;126:224516.

[44] Patzek T, Silin D. Shape factor and hydraulic conductance in noncircular capillaries: I. One-phase creeping flow. Journal of Colloid and Interface Science. 2001;236(2):295-304.

[45] Jacob B. Dynamics of fluids in porous media. Soil Science. 1972.

[46] Gharasoo M, Centler F, Regnier P, Harms H, Thullner M. A reactive transport modeling approach to simulate biogeochemical processes in pore structures with pore-scale heterogeneities. Environmental Modelling & Software. 2012;30:102-114.

[47] Payne TE, Brendler V, Comarmond MJ, Nebelung C. Assessment of surface area normalisation for interpreting distribution coefficients (K d) for uranium sorption. Journal of Environmental Radioactivity. 2011;102(10):888-895.

[48] Freundlich H. Concerning adsorption in solutions. Journal of Physical Chemistry. 1906;57:385.

[49] Grady LJ, Polimeni JR. Discrete calculus: Applied analysis on graphs for computational science. Springer, 2010.

[50] Van Loon L, Soler J, Bradbury M. Diffusion of HTO, $^{36}Cl^-$ and $^{125}I^-$ in Opalinus Clay samples from Mont Terri: Effect of confining pressure. Journal of Contaminant Hydrology. 2003;61(1):73-83.

[51] Pearson F. Opalinus Clay experimental water: A1 type. Version 980318. Technical Report TM-44-98-07. Paul Scherrer Institute, Villigen Switzerland; 1998.

[52] Van Loon L, Eikenberg J. A high-resolution abrasive method for determining diffusion profiles of sorbing radionuclides in dense argillaceous rocks. Applied radiation and isotopes. 2005;63(1):11-21.

[53] Bourg IC, Bourg ACM, Sposito G. Modeling diffusion and adsorption in compacted bentonite: a critical review. Journal of Contaminant Hydrology. 2003;61(1-4):293-302.

[54] Appelo CAJ, Wersin P. Multicomponent diffusion modeling in clay systems with application to the diffusion of tritium, iodide, and sodium in Opalinus Clay. Environmental Science & Technology. 2007;41(14):5002-5007.

[55] Glaus MA, Aertsens M, Appelo CAJ, Kupcik T, Maes N, Van Laer L, Van Loon LR. Cation diffusion in the electrical double layer enhances the mass transfer rates for Sr^{2+}, Co^{2+} and Zn^{2+} in compacted illite. Geochim Cosmochim Acta. 2015;165:376-388.

[56] Lehikoinent J, Muurinen A, Valkiainen M. A Consistance Model for Anion Exclusion and Surface Diffusion. MRS Proceedings: Cambridge Univ Press; 1999. p. 663.

[57] Ochs M, Lothenbach B, Wanner H, Sato H, Yui M. An integrated sorption–diffusion model for the calculation of consistent distribution and diffusion coefficients in compacted bentonite. Journal of Contaminant Hydrology. 2001;47(2):283-296.

[58] Van Schaik J, Kemper W. Chloride diffusion in clay-water systems. Soil Science Society of America Journal. 1966;30(1):22-25.

[59] Leroy P, Revil A. A triple-layer model of the surface electrochemical properties of clay minerals. Journal of Colloid and Interface Science. 2004;270(2):371-380.

[60] Leroy P, Revil A, Coelho D. Diffusion of ionic species in bentonite. Journal of Colloid and Interface Science. 2006;296(1):248-255.

[61] Jougnot D, Revil A, Leroy P. Diffusion of ionic tracers in the Callovo-Oxfordian clay-rock using the Donnan equilibrium model and the formation factor. Geochimica et Cosmochimica Acta. 2009;73(10):2712-2726.

[62] Wersin P, Van Loon L, Soler J, Yllera A, Eikenberg J, Gimmi T, Hernan P, Boisson J-Y. Long-term diffusion experiment at Mont Terri: first results from field and laboratory data. Applied Clay Science. 2004;26(1):123-135.

[63] Bradbury MH, Baeyens B. Porewater chemistry in compacted re-saturated MX-80 bentonite. Journal of Contaminant Hydrology. 2003;61(1):329-338.

[64] Appelo CA, Vinsot A, Mettler S, Wechner S. Obtaining the porewater composition of a clay rock by modeling the in- and out-diffusion of anions and cations from an in-situ experiment. Journal of Contaminant Hydrology. 2008;101(1-4):67-76.

[65] Xiong Q, Jivkov AP, Ahmad SM. Modelling reactive diffusion in clays with two-phase-informed pore networks. Applied Clay Science (under revision). 2015.